

Article

Dependence of Electrochemical Characteristics of a Biodegradable Fe-30Mn-5Si wt.% Alloy on Compressive Deformation in a Wide Temperature Range

Pulat Kadirov ^{1,*}, Yury Pustov ², Yulia Zhukova ³, Maria Karavaeva ¹, Vadim Sheremetyev ¹, Andrey Korotitskiy ⁴, Alexandra Baranova ¹ and Sergey Prokoshkin ¹

¹ Metal Forming Department, National University of Science and Technology “MISIS”, 119049 Moscow, Russia; karavaeva.ma@yandex.ru (M.K.); sheremetyev@misis.ru (V.S.); baranova.al.pavlovna@yandex.ru (A.B.); prokoshkin@tmo.misis.ru (S.P.)

² Department of Steel Metallurgy, New Production Technologies and Protection of Metals, National University of Science and Technology “MISIS”, 119049 Moscow, Russia; pustov@misis.ru

³ Center of Nanomaterials and Nanotechnologies, National University of Science and Technology “MISIS”, 119049 Moscow, Russia; zhukova@misis.ru

⁴ Ultrafine-Grained Metallic Materials Laboratory, National University of Science and Technology “MISIS”, 119049 Moscow, Russia; akorotitskiy@gmail.com

* Correspondence: pulat_1993-2009@mail.ru

Abstract: Fe-30Mn-5Si alloy subjected to a compression test at various deformation temperatures ranging from 350 to 900 °C with a strain rate of 1 s⁻¹ are studied. It was found that the Fe-30Mn-5Si alloy exhibits high resistance to the dynamic recrystallization process in a whole studied range of deformation temperatures. There are no differences in structure formation in the zone of action of tangential tensile stresses and peripheral and central zones of localized compressive stresses. The room-temperature X-ray diffraction study shows the presence of a single-phase state (FCC γ -austenite) after deformation temperature range from 350 to 700 °C and a two-phase state (FCC γ -austenite + HCP ϵ -martensite) after deformation test at 900 °C. The presence of a two-phase state provides a higher rate of biodegradation compared with a single-phase state. The changes in the biodegradation rate dependence on the structure change with an increase in the deformation temperature are explained. Favorable temperature regimes for subsequent thermomechanical processing are proposed based on the relationship between structure formation and biodegradation rate to obtain semi-products from the Fe-30Mn-5Si alloy.

Keywords: biodegradable shape memory alloys; electrochemical behavior; thermomechanical treatment; rheological behavior; grain structure; phase composition



Citation: Kadirov, P.; Pustov, Y.; Zhukova, Y.; Karavaeva, M.; Sheremetyev, V.; Korotitskiy, A.; Baranova, A.; Prokoshkin, S. Dependence of Electrochemical Characteristics of a Biodegradable Fe-30Mn-5Si wt.% Alloy on Compressive Deformation in a Wide Temperature Range. *Metals* **2023**, *13*, 1830. <https://doi.org/10.3390/met13111830>

Academic Editor: Xiaobo Zhang

Received: 19 September 2023

Revised: 26 October 2023

Accepted: 27 October 2023

Published: 31 October 2023



Copyright: © 2023 by the authors. Licensee MDPI, Basel, Switzerland. This article is an open access article distributed under the terms and conditions of the Creative Commons Attribution (CC BY) license (<https://creativecommons.org/licenses/by/4.0/>).

1. Introduction

In the past two decades, there has been a growing interest in biodegradable metallic materials for use as temporary devices in traumatology, osteosynthesis, orthopedics, and cardiovascular surgery [1–7]. Magnesium (Mg), zinc (Zn), iron (Fe), and some of their alloys are the most favorable candidates for these applications [8–14]. Among these biodegradable alloys, Fe-based alloys appear to be the most promising ones due to their excellent combination of mechanical properties, similar to stainless steels [15], sufficient biocompatibility [16,17], as demonstrated by in vivo experiments [18,19], and the absence of hydrogen release during the biodegradation process. However, Fe-based alloys exhibit a low biodegradation rate. In order to increase the electrochemical activity, iron is alloyed with manganese (Mn), whose electrode potential is much lower (−1.18 V) than that of pure Fe (−0.44 V) [20]. The further increase in the biodegradation rate and mechanical properties is achieved by adding silicon (Si) to Fe-Mn binary alloys, which form non-metallic inclusions of SiO₂ acting as cathode structural components, increasing the biodegradation

rate. The enhancement of biodegradation rate can also be increased by adding nitrogen (N) to the alloys of the Fe-Mn system. The authors found [21] that N addition (0.3 . . . 0.6 wt.%) leads to a significant increase in the corrosion rate of the Fe-30Mn alloy in both Hank's solution and simulated gastric fluid.

The Fe-Mn-Si alloys exhibit a shape memory effect due to the reversible martensitic transformation FCC γ -austenite \leftrightarrow HCP ϵ -martensite. In these alloys, which are intended for use as potential materials for bone implants, it is advisable to consider only the temperature of the start of forward $\gamma \rightarrow \epsilon$ martensitic transformation (M_s) since near the temperature M_s pre-transition crystal lattice softening effect takes place, which leads to a decrease in Young's modulus, thus increasing the biomechanical compatibility. According to [22], Fe-Mn-Si alloy containing from 28 to 33 wt.% Mn and from 4 to 6 wt.% Si exhibits a nearly perfect shape memory effect. In [23], Fe-Mn-Si alloys with different Mn content were studied. It was shown that Fe-30Mn-5Si (hereinafter in wt.%) exhibits the most appropriate combination of functional properties: biodegradation rate (0.8 mm/year); Young's modulus (118 GPa); and M_s (50 °C) temperature close to human body temperature.

The subsequent studies were focused on improving the mechanical properties and biomechanical compatibility of the Fe-30Mn-5Si alloy by means of thermomechanical treatment (TMT). The best combination of functional properties was achieved by hot longitudinal rolling at 800 °C with a true strain of $\epsilon = 0.3$, resulting in a dynamically recrystallized structure with an average grain size of about 100 μm [24,25]. This TMT mode resulted in the M_s temperature lowering to the human body temperature (38 °C), achieving high mechanical properties (ultimate tensile strength 725 MPa, apparent yield stress 260 MPa, Young's modulus about 120 GPa, elongation to failure about 15%), suitable biodegradation rate of 0.5-mm/year, and high functional fatigue characteristics both in normal conditions in an air atmosphere and Hanks' solution. However, all these experiments were carried out in laboratory conditions involving small-size specimens. Moreover, the possibilities of TMT to form fine-grained, particularly ultra-fine-grained (UFG) structures in the long semi-products have not been investigated yet.

The conventional methods to obtain long semi-products with fine-grained and UFG structures include radial-shear rolling, multiaxial forging, and longitudinal rolling. These methods show excellent combinations of functional properties for Ti-, Al-, Mg-, and Fe-based alloys [26–37]. However, to determine the favorable temperature-rate conditions for implementing the above-mentioned TMT processes, it is necessary to carry out the rheological tests in wide temperature and strain rate ranges. For example, Zambrano et al. [38] studied the deformation behavior of Fe-Mn-Si-C alloys in the temperature range from 800 °C to 1050 °C with strain rates of 0.01, 0.1, and 1 s^{-1} . They found that in all cases, a dynamic recrystallization process was observed, accompanied by a decrease in the stress peak. Additionally, it was shown that at the same deformation temperature, such as 900 °C, an increase in the strain rate resulted in a higher amount of recrystallized grains. It is important to note that the process of dynamic recrystallization is accompanied by a non-uniform distribution of the applied external load, which can lead to the formation of various defects in the semi-products. In this regard, our previous work aimed at the study of the deformation behavior, structure formation, and mechanical properties of Fe-30Mn-5Si alloy subjected to the compression test in a wide deformation temperature range from 250 to 900 °C, and strain rates of 0.1, 1, and 10 s^{-1} [39]. Based on the relationship between the structure formation and the shape of obtained stress-strain diagrams, favorable regimes for subsequent radial-shear rolling, multiaxial forging, and longitudinal rolling were formulated: deformation temperature of 900 °C and a strain rate of 1 s^{-1} [39].

The biodegradation rate is one of the most important functional properties of materials designed for biodegradable bone implants. Therefore, the study of the Fe-30Mn-5Si alloy electrochemical behavior in relation to the structure formed after the rheological test in a wide deformation temperature range and strain rate of 1 s^{-1} deserves its own study. At this moment, there are no studies on the effect of the structure formed as a result of the rheological tests (compression test) on the electrochemical behavior of biodegradable

Fe-Mn-Si alloys. Thereon, the objective of this work was to study the relationship between the structure formation and the electrochemical behavior of biodegradable Fe-30Mn-5Si shape memory alloy subjected to compression tests in a wide range of temperatures.

2. Materials and Methods

The 12 kg ingot of 80 mm diam. and approximately 250 mm in length ingots of experimental Fe-30Mn-5Si alloy were produced by vacuum induction melting. The chemical composition and element distribution of elements were controlled by atomic emission spectroscopy with inductively coupled plasma and X-ray spectroscopy using a JEOL JSM-6480 LV (Jeol, Echting b. München, Germany) scanning electron microscope in different parts of the ingots. After verifying the chemical composition, the studied Fe-30Mn-5Si alloy was subjected to reference heat treatment (RHT), including homogenization annealing at 900 °C for 60 min and subsequent water cooling to avoid an as-cast structure [23,24,40]. The electrical discharge technique was used to cut 15 mm long and 10 mm diam. specimens for subsequent rheological compression tests.

In the compression tests (plastometry tests), the specimens were deformed up to the true (logarithmic) strain of $e = 0.7$ at a strain rate of 1 s^{-1} and temperatures of 350, 500, 700, and 900 °C using high-precision simulation laboratory equipment—Gleeble System 3800 (Dynamic Systems Inc., Austin, TX, USA) equipped with the *Hydrawedge-II* high-temperature compression test module with auxiliary devices for registration and control of temperature, force, displacement, and strain rate. The compression test was carried out with the vacuumed work chamber of at least 10^{-5} atm to avoid the specimen's oxidation. To reduce the contact friction forces between the end surfaces of the samples and the deforming working surfaces of the strikers made of tungsten carbide, grease based on nickel, graphite, boron nitride, or special graphite foil was used. To prevent “sticking” of the samples to the striker surface, tantalum foil was placed between their contact areas. The studied Fe-30Mn-5Si specimens were directly heated by the controlled electric current application. This method provides fast heating and uniform heat distribution over the entire samples' volume. Upon completion of the compression tests, the specimens were air-cooled at a rate of 20 °C/s.

After compression tests, the specimens were cut along the load direction for subsequent study of the structure by optical microscopy, X-ray analysis, and electrochemical studies. After cutting, the specimens were ground with P 320 to P 4000 emery paper and further mirror-polished with diamond suspension. To reveal the structure, a solution of nitric acid in ethanol with a ratio of 4:96 wt.%, respectively, was used as an etchant. Three zones were studied in each specimen: the zone of action of tangential tensile stresses (zone A); the peripheral zone (Zone B); and the central zone (Zone C) of localized compressive stresses [41].

The X-ray diffraction (XRD) analysis was carried out at room temperature using a DRON-3 (Burevestnik Innovation Centre, St. Petersburg, Russia) diffractometer with $\text{CuK}\alpha$ radiation ($\lambda = 0.154178 \text{ nm}$). The studied 2θ -angle range from 30 to 100 deg. was scanned with 0.1 2θ deg. step and 3 s for exposure. A graphite monochromator was used for noise level lowering. In order to remove the stress-induced martensite formed by specimens' preparation, chemical etching was used. The thickness of the removed layer was 0.5 mm.

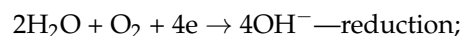
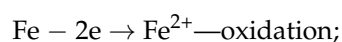
An electronic IPC-Pro potentiostat with a three-electrode 200 mL glass cell was used for electrochemical study to measure open circuit potential (OCP) and potentiodynamic polarization curves. During the electrochemical tests, a constant temperature of 37 °C was maintained using a TW-2 Elmi (ELMI Ltd., Riga, Latvia) thermostat. Hanks' solution, simulating the inorganic composition of bone tissue medium, was used as the electrolyte [24,25]. To ensure stable electrical contact, a copper wire was soldered to the studied specimens, with the subsequent embedment in epoxy resin. Then, samples were further ground with P320 to P1200 emery paper. The working area for the electrochemical experiment was 25 mm^2 . Each electrochemical experiment was carried out at 37 °C and repeated at least three times to ensure reproducibility of the results. The exposure time of the samples to

obtain steady-state OCP values was 7000 s. The polarization diagrams were obtained from the cathodic region, ranging from 250 mV negative to the OCP value of the studied alloy. The top potential values were approximately 100 mV more positive compared to the OCP values. The potential sweep rate for the polarization test was 0.2 mV/s. The saturated Ag/AgCl₂ electrode was used as the reference electrode, and the platinum one served as an auxiliary electrode. For the corrosion rate (C_r) estimation, the corrosion current density (i_{corr}) was extrapolated from the polarization curves as follows [42]:

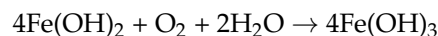
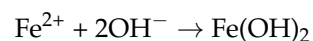
$$C_r = \frac{i_{corr} 10^4 A_{Me}}{n F d_{Me}} 8.76 \text{ mm/year} \quad (1)$$

where i_{corr} is the corrosion current density, A/cm²; n —is ionic charge ($n = 2$ for Fe²⁺); $F = 26.8$ A·h/gram-equivalent is the Faraday constant; A_{Me} is the atomic weight of metal, g; d_{Me} is the metal density, g/cm.

The choice to use the method of corrosion rate estimation by extrapolation of the potentiodynamic polarization curves using Equation (1) is justified by the following factors. Firstly, Equation (1) is widely used to calculate the biodegradation rate of metals and alloys corroding in active dissolution mode. Secondly, previous studies conducted by the authors of this manuscript have shown that long-term corrosion testing, as described in ASTM G31-21 [43], results in the accumulation of corrosion products on the sample surface and in the electrolyte volume. However, in real conditions during the process of biodegradation and bone tissue regeneration, there is a constant release of low-valence ions, such as Fe²⁺ and Mn²⁺ (typical for the corrosion of these metals in neutral media), which prevents the formation of solid precipitates as corrosion products on the implant surface. The authors of this manuscript have previously conducted corrosion tests using this standard method. However, the corrosion rate calculated based on the mass loss of the samples was much lower than the corrosion rate of the Fe-30Mn-5Si alloy obtained by extrapolating polarization curves. Analysis of the samples with the X-ray photoelectron spectroscopy showed that after ASTM G31-21 testing, corrosion products in the form of iron (Fe₂O₃, Fe₃O₄, FeOOH) and manganese (MnO) compounds were present on the surface of the samples, with the most abundant Fe²⁺ peaks being most common in the Fe₃O₄ multiplet. It is known that the corrosion of iron in neutral media proceeds through oxygen depolarization. The anodic and cathodic processes are shown below, respectively [42,44,45]:



The following reactions take place on the metal surface in the test at full immersion in the electrolyte:



3. Results and Discussion

3.1. Structure and Phase Analysis

Figure 1 shows optical microscopy images of the Fe-30Mn-5Si alloy after the reference heat treatment (RHT), which provides a homogeneous state of chemical composition and structure [23–25]. As can be seen, the Fe-30Mn-5Si alloy consists of γ -austenite grains with an average grain size of about 200–300 μm with chaotic shape and ε -martensite plates inside some of the grains. In some areas, smaller equiaxed grains are observed.

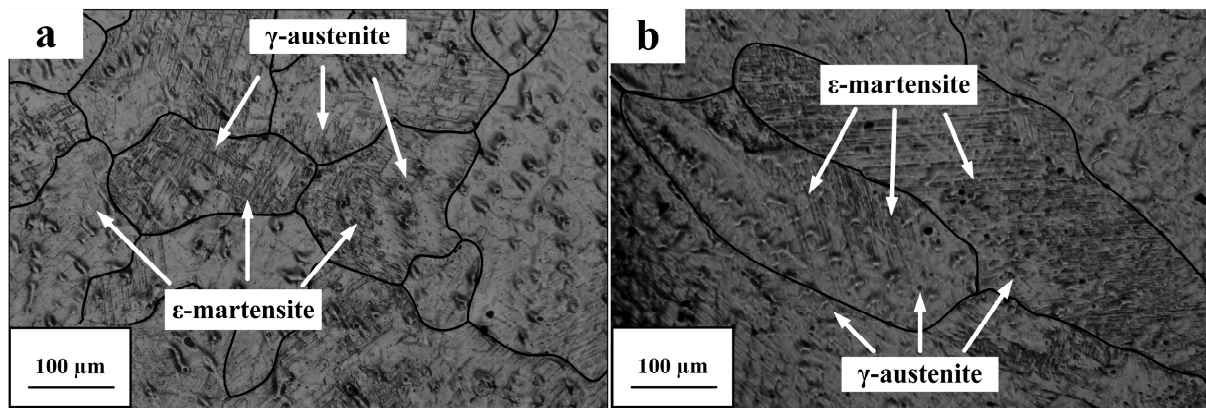


Figure 1. Typical optical microstructure images of the Fe-30Mn-5Si alloy after RHT were taken from various areas of specimens: (a) grains with average size of 200 μm ; (b) grains with average size of 300 μm .

Figure 2 shows the optical microscopy images of the Fe-30Mn-5Si alloy after the compression tests at 350, 500, 700, and 900 $^{\circ}\text{C}$ with the strain rate of 1 s^{-1} . It can be observed that, regardless of the studied zone and deformation temperature, the grains' shape changes, and their size becomes smaller along the deformation axis and larger in the perpendicular direction, which could indicate the absence of the dynamic recrystallization process and, consequently, the presence of the dynamic polygonization process. A similar state is observed up to 900 $^{\circ}\text{C}$. It is noteworthy to note that there are no differences in structure formation between the three studied zones. This indicates a uniform strain distribution during compression testing. One of the main characteristics that can be observed from Figure 2 is the absence of equiaxed recrystallized grains in all studied zones and deformation temperatures up to 900 $^{\circ}\text{C}$, which probably indicates high resistance of the Fe-30Mn-5Si alloy to the development of dynamic recrystallization processes up to high temperatures. However, starting at the deformation temperature of 700 $^{\circ}\text{C}$ zone A and zone B (Figure 2g,h), the grains with smaller size (about 100–200 μm) can be observed. At first, it might be assumed that it is the result of partial recrystallization. However, after the deformation at 900 $^{\circ}\text{C}$, only non-recrystallized grains are observed, which indicates the impossibility of the process of dynamic recrystallization at lower deformation temperature (700 $^{\circ}\text{C}$). Thus, the smaller non-equiaxed grains in Figure 2g,h at temperature 700 $^{\circ}\text{C}$ are the deformed smaller grains that remained after the RHT regime (Figure 1). It is important to note that the dynamic recrystallization process during thermomechanical treatment can cause a non-uniform structure formation. This may result in uneven load application and lead to the destruction of test specimens.

Figure 3 shows the X-ray diffractograms of the Fe-30Mn-5Si alloy after the RHT and compression test in the deformation temperature range from 350 to 900 $^{\circ}\text{C}$ with a strain rate of 1 s^{-1} . In the diffraction patterns of the Fe-30Mn-5Si alloy after the RHT regime, the presence of two phases, FCC γ -austenite and HCP ϵ -martensite, is observed. Note that after compression tests in the deformation temperature range from 350 to 700 $^{\circ}\text{C}$, only a single FCC γ -austenite phase is present. This may be related to the fact that after the deformation with true logarithmic strain $e = 0.7$ in the above-mentioned deformation temperature range, the temperature of the start of forward martensitic transformation $\gamma \rightarrow \epsilon$ (M_s) falls below room temperature. It is noteworthy that the M_s temperature after the RHT is about 21 $^{\circ}\text{C}$ [39]. In this regard, the true logarithmic strain of $e = 0.7$ should be enough to decrease the M_s below room temperature due to the formation of a highly dislocated substructure, and correspondingly, the ϵ -martensite phase is absent in the X-ray diffractograms obtained at room temperature. It is also necessary to note the absence of iron carbide (Fe_{23}C_6 or Fe_3C) lines in the X-ray diffractograms; this will be important for the discussion of the subsequent electrochemical experiments' results. However, weak

ϵ -martensite is observed in the X-ray diffractograms taken after the deformation at 900 °C (Figure 4), which indicates that at this deformation temperature, the softening processes (dynamical recovery and polygonization) prevail over the hardening process. Therefore, the M_s temperature remains above room temperature.

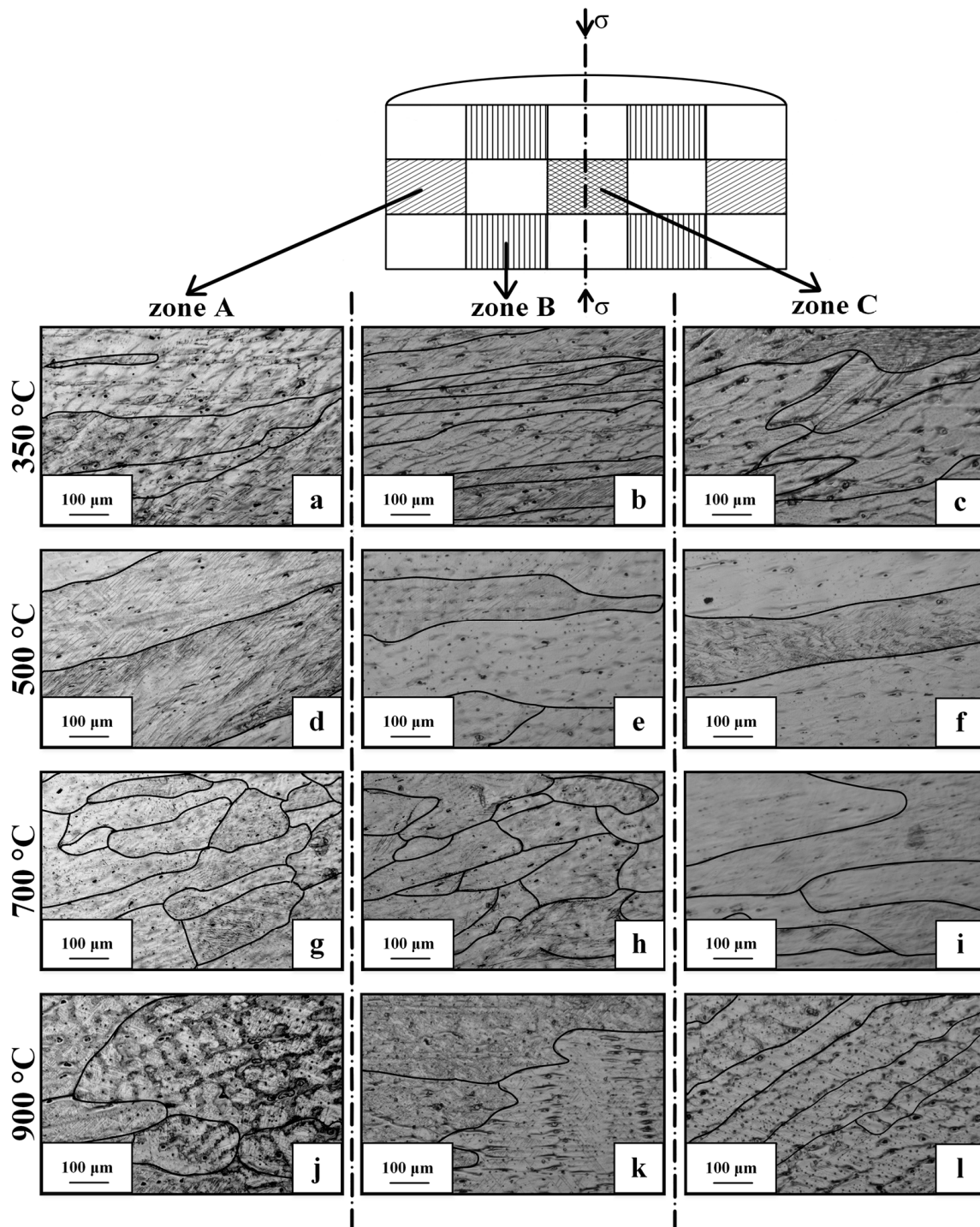


Figure 2. Schematic representation of different zones (the arrow indicates the load axis) and optical microscopy images of the Fe-30Mn-5Si alloy microstructure after compression test at strain rate 1 s^{-1} and deformation temperatures of 350 °C (a–c), 500 °C (d–f), 700 °C (g–i), and 900 °C (j–l) in zone A (zone of action of tangential tensile stresses), zone B (peripheral zone of localized compressive stresses), and zone C (central zone of localized compressive stresses).

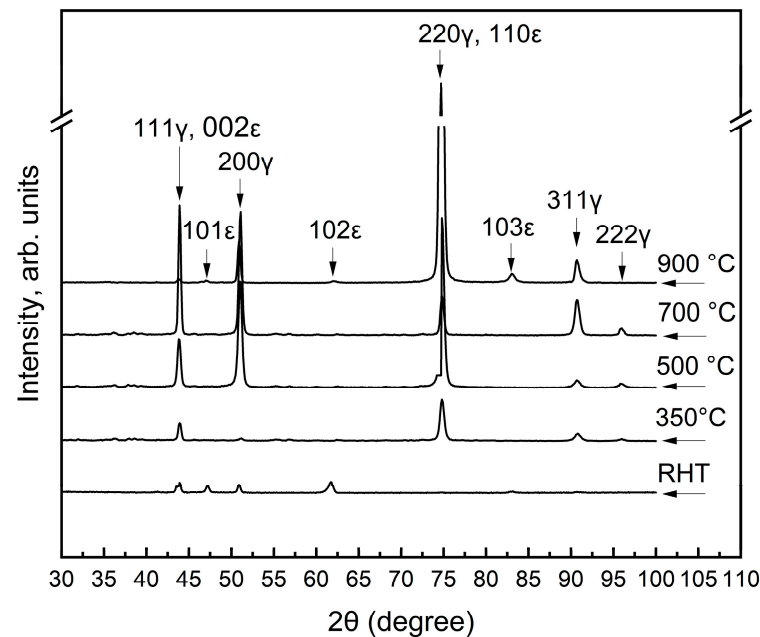


Figure 3. X-ray diffractograms of the Fe-30Mn-5Si alloy after RHT and compression tests in temperature range from 350 to 900 °C.

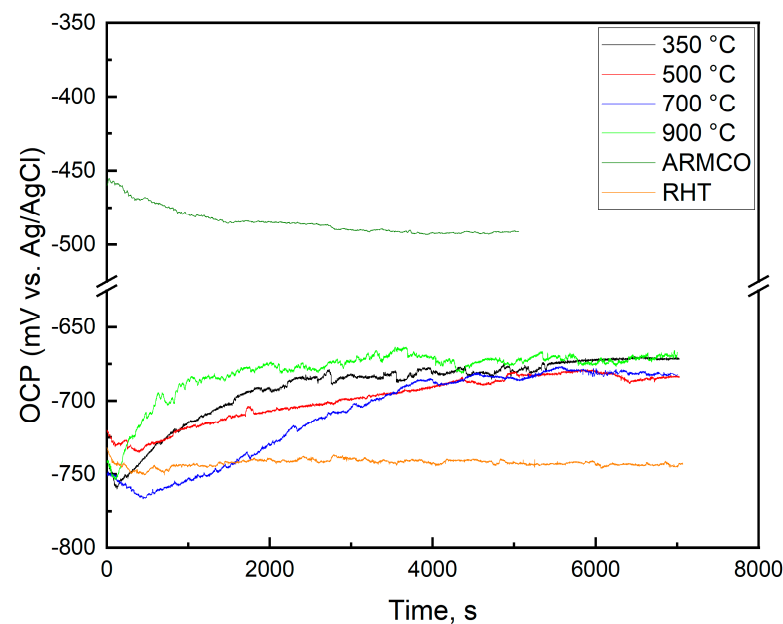


Figure 4. OCP curves of the Fe-30Mn-5Si alloy after compression test obtained at temperatures of deformation of 350, 500, 700, and 900 °C and strain rate 1 s^{-1} immersed in Hanks' solution at 37 °C.

Table 1 shows the half-height width of $\{200\}\gamma$ ($B200_\gamma$) X-ray diffraction line after the RHT and compression tests. According to Table 1, the RHT produces a less broadening of the $\{200\}\gamma$ X-ray line than alloy after compression tests at deformation temperatures from 350 to 700 °C, similar to deformation temperature of 900 °C. This confirms the presence of a more developed dislocation substructure and, consequently, the absence of the ϵ -martensite phase due to the above-described mechanism. The decrease in the γ -austenite X-ray line width $B200_\gamma$ is associated with the reduction in crystal lattice defect concentration via softening processes, such as dynamic recovery and dynamic polygonization in the dislocation substructure. With the increase in deformation temperature, the formation of subgrains with low-angle ($<15^\circ$) sub-boundaries occurs. The higher the deformation

temperature, the lower the density of free dislocations in the subgrain bodies, and the larger the subgrain size, which leads to a decrease in the X-ray line broadening [39].

Table 1. X-ray line half-height width $B_{200\gamma}$ of Fe-30Mn-5Si alloy after RHT and compression tests at deformation temperatures 350–900 °C with strain rate 1 s^{-1} .

RHT and TMT Regimes	$B_{200\gamma}$, 2 θ deg.
RHT	0.39 ± 0.02
350 °C	0.51 ± 0.03
500 °C	0.50 ± 0.03
700 °C	0.43 ± 0.03
900 °C	0.39 ± 0.02

3.2. Electrochemical Behavior

The electrochemical behavior of the Fe-30Mn-5Si alloy was studied in Hanks' solution at 37 °C after the compression tests at deformation temperatures of 350 °C, 500 °C, 700 °C, and 900 °C and strain rate 1 s^{-1} . In order to clarify the features of the alloy's electrochemical behavior after compression tests, the RHT specimens, as well as pure ARMCO Fe, were also tested for comparison.

Figure 4 shows the OCP curves of the Fe-30Mn-5Si alloy after compression tests, RHT, and pure ARMCO Fe. As can be seen, during the exposure in the solution, the OCP curves of pure Armco Fe monotonically shift down toward the negative value until the stationary value is established (-480 mV). Moreover, with the general tendency of its change on polarization curves, small fluctuations of the potential within $\pm 3 \text{ mV}$ are observed, which reflect the processes that occur on the surface of the specimens. Thus, potential shifts to the negative direction (cathodic polarization) can be associated with the filling of primary pores in the film of corrosion products with electrolyte, resulting in an increase in the area of the metal in contact with the solution. The further anodic polarization is associated with the formation of corrosion products in the pores, which shield the metal surface from the electrolyte. The subsequent potential shifts in the negative direction can be associated with the destruction of the corrosion product film and the formation of secondary pores. In the steady-state stage, OCP fluctuates around a certain value, which reflects the stationary state of the corrosion process.

The observed OCP kinetics is characteristic of metals that corrode in active mode. Pure ARMCO Fe contains a small amount of cementite (Fe_{23}C_6 or Fe_3C [40]), which acts as an effective cathodic structural component. During the exposure, corrosion products (iron hydroxides) form on the surface of the studied specimens [46], which impedes the access of the depolarizer (dissolved oxygen) to the cathode areas of the surface and leads to the inhibition of the cathodic depolarization process due to the diffusion overvoltage generation and, as a result, to a negative potential shift and the decrease in the corrosion rate.

The steady-state OCP values of the Fe-30Mn-5Si alloy, after all studied TMT modes, exhibit much more negative values ($-675 \pm 7 \text{ mV}$), which is obviously due to the presence of strongly electronegative Mn (the standard electrode potential of the $\text{Mn} \leftrightarrow \text{Mn}^{2+} + 2e$ reaction is -1.18 V) in the alloy composition. The corrosion of the Fe-30Mn-5Si alloy also proceeds by the active dissolution mode; however, the nature of the OCP changing during the exposure, in this case, indicates some specific corrosion process features. In all cases, in the initial period of exposure (100–200 s), there is a slight but quite noticeable OCP shift toward the negative values, which indicates a similar nature of the effect of primary corrosion products.

In this case, the OCP values of the RHT specimens after the initial cathodic polarization are established at a value of $-748 \pm 2 \text{ mV}$ and are stable during further exposure. At the same time, alloy specimens after the compression test experience anodic polarization of

more than 100 mV. Such behavior of the alloy is related to its fully austenitic (FCC γ -phase) structure after all modes of compression testing. The exception is the specimens after the compression test at 900 °C, after which (according to the results of X-ray phase analysis, Section 3.1) a small amount of the HCP ϵ -martensite phase is formed, which acts as the anodic structural component [24,47]. However, this does not alter the overall OCP change trend during the exposure. The absence of the ϵ -martensite in the alloy (or its low content) suggests that active grain boundaries, subgrains, and subgrains themselves will act as the main anode structural component, which should lead to their selective dissolution. This should lead to a relative increase in the cathode γ -austenite area fraction and, consequently, the accelerated cathodic process and a corresponding corrosion rate increase with the observed potential shift towards the positive direction.

After undergoing the RHT, the Fe-30Mn-5Si alloy exhibits a two-phase structure consisting of γ -austenite and ϵ -martensite, with a higher volume fraction of the ϵ -martensite phase [40,44,48,49]; therefore, the “cathode efficiency” of γ -austenite is less manifested, and the corrosion process occurs mainly by ϵ -martensite phase dissolution. It should be noted that both for the Fe-30Mn-5Si alloy and for pure Fe, the process of establishing the steady-state corrosion stage, the potential fluctuations are observed, but in the case of Fe-30Mn-Si alloy, the oscillation magnitude reaches 20 mV. Larger OCP fluctuations may indicate the formation of more friable corrosion products with low adhesion and, accordingly, poor protection ability.

It also seems appropriate to consider another option to justify the spontaneous anodic polarization observed during the exposure of the alloy specimens after all modes of the compression test. In theory, the formation of sustainable corrosion products exhibiting even minor protective ability can lead to inhibition of the anodic process and, accordingly, to the corrosion rate decrease. The structure of the alloy after compression testing is represented only by the cathodic γ -austenite, and the active grain and subgrain boundaries [39], which occupy an insignificant part of the surface area compared to the area of the grains themselves, act as the anodic structural component. Since the anodic process turns out to be highly localized, it is impossible to cover the predominant part of the specimen surface with corrosion products. But, due to the metal atom ionization becoming largely inhibited, we should expect the anodic process to slow down and, therefore, spontaneous anodic polarization to take place. However, this explanation contradicts the data obtained for the RHT mode. Since the anodic structural component (ϵ -martensite) dominates in the two-phase structure of the alloy after RHT, the corrosion products should occupy a significant part of the specimen surface during the dissolution process. This should lead to a significant inhibition of the anodic process and cause a large OCP shift toward the positive direction. However, according to Figure 4, the OCP value of the RHT is almost constant during the exposure and is about -750 mV, which is 50–70 mV lower than the steady-state OCP values of the alloy after compression tests. The inconsistency of such an explanation for the observed regularities of OCP changes during the exposure is supported by the results of the corrosion current density measurements presented below, according to which the highest corrosion rate is achieved for the alloy right after RHT.

Figure 5 shows the potentiodynamic polarization diagrams of pure ARMCO Fe and Fe-30Mn-5Si alloy after compression tests and RHT mode. It can be seen that regardless of the test mode, there is a similar pattern of OCP change upon the potential application. The anodic and cathodic branches of the polarization curves represent, respectively, the reaction of the dissolution of metal (alloy) atoms and the reaction involving oxygen in the depolarization process. A significant slope of the cathodic (lower) branches of the polarization curves indicates that the corrosion process, in all cases, proceeds with cathodic control. The cathodic process in neutral media is described by the following reaction:



which is the sum of sequential elementary reactions, four of which are electrochemical with the participation of one electron in each [42,44,45]. It is believed that the rate-limiting stage of the process is the formation of a molecular oxygen ion by an electrochemical reaction



whose slowness causes the cathodic process overvoltage. As follows from the polarization diagrams plotted in the Tafel representation (Figure 5), the cathodic branches are straight lines in a wide potential range, with the same slope b of the Tafel equation, accounting for 0.2 ± 0.01 , but with different cathode current densities under the same applied polarization potentials. Taking into account that the mechanism of the cathode process is the same, one can indicate the difference in kinetic parameters.

$$b = \frac{RT}{anF} \cdot 2.303; \quad (4)$$

where $R = 8.314 \frac{\text{J}}{\text{mol} \cdot \text{K}}$; T is the temperature, K; a is the charge transfer coefficient; n is the number of electrons involved in the reaction; $F = 96,500 \frac{\text{C}}{\text{g-equivalent}}$, Faraday constant.

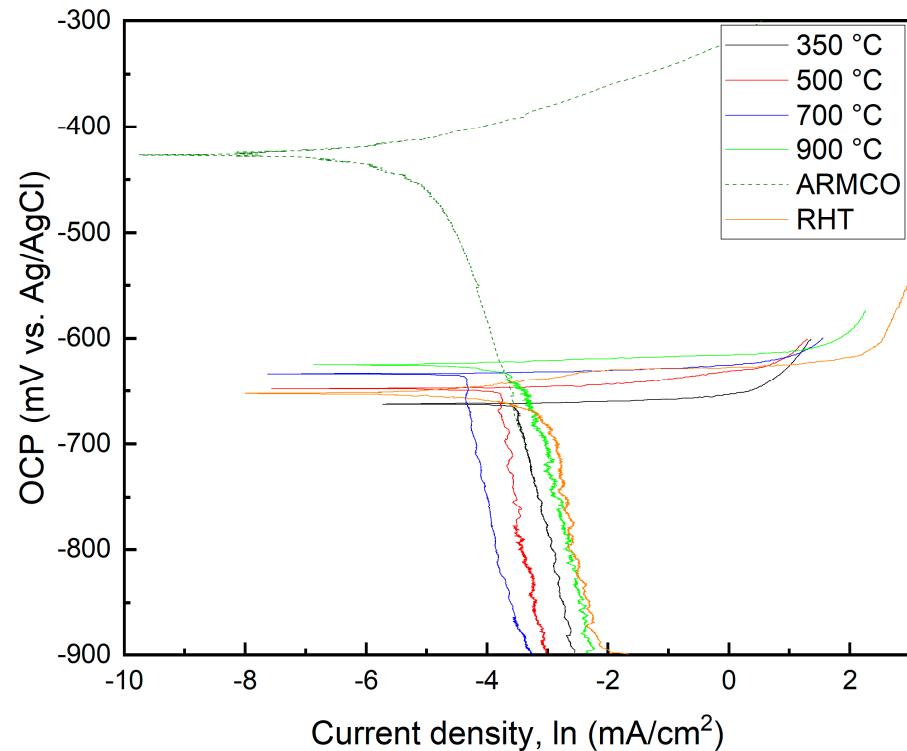


Figure 5. Polarization diagrams of the Fe-30Mn-5Si alloy immersed in Hanks' solution at 37 °C after compression tests at deformation temperatures 350, 500, 700, and 900 °C and strain rate of 1 s^{-1} .

Considering that $n = 1$ and $T = 310 \text{ K}$, the charge transfer coefficient for the cathodic reaction is $\alpha = 0.3 \pm 0.01$, as follows from Equation (4). The α coefficient characterizes the degree of impact of the electrode electric field on the activation energy of the electrochemical stage, and the obtained value indicates the asymmetry of the activation barrier of the electrochemical reaction.

The electrochemical parameters of Fe-30Mn-5Si alloy specimens after compression tests and the RHT mode, compared to pure ARMCO Fe, obtained by extrapolation of the Tafel parts of the polarization curves in Hanks' solution at 37 °C, are listed in Table 2.

Table 2. The electrochemical parameters of Fe-30Mn-5Si alloy specimens after compression tests and the RHT mode, compared to pure ARMCO Fe, obtained by extrapolation of the Tafel parts of the polarization curves in Hanks' solution at 37 °C.

Treatment	Corrosion Potential E_{corr} , mV	$i_{corr} \cdot 10^5$, A/cm ²	Corrosion Rate *, Cr, mm/year
compression test temperature 350 °C	-663 ± 5	2.75 ± 0.16	0.33
compression test temperature 500 °C	-648 ± 4	2.11 ± 0.1	0.25
compression test temperature 700 °C	-633 ± 6	1.24 ± 0.09	0.14
compression test temperature 900 °C	-625 ± 4	3.58 ± 0.14	0.42
RHT	-653 ± 7	5.11 ± 0.26	0.6
Pure ARMCO Fe	-427 ± 3	0.85 ± 0.05	0.10

* Calculated values according to the Equation (1).

As can be seen from Table 2, the following regularity takes place: for Fe-30Mn-5Si alloy after compression tests, with an increase in deformation temperature from 350 to 900 °C, the corrosion potential shifts toward the positive values, which indicates a decrease in the electrochemical activity of the alloy; at the same time, the expected decrease in the corrosion current density is observed only with an increase in the deformation temperature to 700 °C, while deformation at 900 °C, on the contrary, leads to a significant increase in the corrosion current density despite the apparent higher thermodynamic (electrochemical) stability of the studied alloy.

The observed trends in the electrochemical parameters are related to the structure of the specimens. As shown above, the structure of Fe-30Mn-Si alloy after compression tests in the temperature range from 350 to 700 °C is characterized by the single-phase state (FCC γ -austenite). However, the observed changes in E_{corr} and i_{corr} indicate the necessity to consider the structural features that affect the electrochemical characteristics of the alloy. The compression test at the temperature of 350 °C is accompanied by the formation of a dynamically polygonized dislocation substructure in the deformed grains of the γ -austenite matrix, characterized by an increased density of dislocations in the subgrain body. The strongest broadening of the X-ray lines also indicates the most strengthened state of the structure (Table 1). With an increase in the temperature of compression tests to 500 and 700 °C, dynamic recovery is observed, leading to a decrease in the concentration of point defects and a decrease in dislocation density not associated with the formation and movement of grain boundaries and dynamic polygonization—redistribution of dislocations by slip and diffusion, which is accompanied by their partial annihilation and the formation of subgrains inside crystallites free of dislocations [39,50,51]. The observed changes in the state of the structure cause an “elevation” of the potential and a decrease in the corrosion rate.

The electrochemical parameters of specimens after compression test at 900 °C are influenced by two factors: (1) the ongoing process of dynamic recovery and dynamic recrystallization, accompanied by the formation of fine equiaxed grains, which should cause further “elevation” of the corrosion potential; (2) the appearance of an additional anodic phase— ϵ -martensite in the structure of the specimen, which should lead to an increased corrosion rate. However, judging by the significant increase in the corrosion current density, in this case, the determining factor in the electrochemical behavior of the specimens is the appearance of the ϵ -martensite. This is indicated by the electrochemical parameters of the RHT mode, which is in a two-phase (γ -austenite and ϵ -martensite) state of the structure, in which the ϵ -phase predominates. The present data correlate well with

studies of the Fe-29Mn-5Si alloy, which also contains only FCC γ -austenite phase and consequently has a corrosion rate in the range of 0.21–0.25 mm/year [52].

4. Conclusions

1. The theoretical justification for the atypical changes in the electrode potential during the exposure of the Fe-30Mn-5Si alloy, which corrodes via active dissolution mode in a biological solution, was provided. It is shown that the cause of the spontaneous anodic polarization of the Fe-30Mn-5Si alloy after compression tests at temperatures of 350, 500, 700, and 900 °C is the absence (or low content) of the anodic structural component (HCP ϵ -martensite) after the compression test at 900 °C. Wherein the active grains and subgrains boundaries, and subgrains themselves act as the anodic structural components, with their selective dissolution increasing the relative amount of cathodic structural components on the surface of the studied specimens that leads to an accelerated cathodic process and corresponding increase in biodegradation rate with an observed shift toward the positives values of the electrode potential;
2. The biodegradation rates of the Fe-30Mn-5Si alloy were calculated using the extrapolation method of polarization curves after compression tests at deformation temperatures of 350, 500, 700, and 900 °C and a strain rate of 1 s⁻¹. The analysis of polarization curves allowed for the establishment of the causes and patterns of changes in the electrochemical parameters of the studied alloy, depending on the thermomechanical treatment regimes. The observed elevation of the corrosion potential and the decrease in the corrosion current density of the Fe-30Mn-5Si alloy after compression tests at the deformation temperatures of 350, 500, and 700 °C, which consist only of the FCC γ -austenite phase, are due to dynamic recovery, which leads to a decrease in the concentration of point defects, and dynamic polygonization;
3. Based on the results of the rheological compression tests, taking into account the biodegradation rate of the Fe-30Mn-5Si alloy, the radial–shear rolling, multiaxial forging, and longitudinal rolling should be carried out at a deformation temperature of 900 °C and strain rate of 1 s⁻¹ due to the following reason: these chosen deformation conditions result in a two-phase state, comprising FCC γ -austenite + HCP ϵ -martensite, which provides the highest biodegradation rate. It is worth noting that the results of this study on electrochemical behavior established that thermomechanical treatment at a specific deformation temperature from 350 to 900 °C and strain rate 1 s⁻¹ can regulate the biodegradation rate of the Fe-30Mn-5Si alloy, which ranges from 0.14 to 0.42 mm/year, depending on the desired recovery rate for damaged bone tissue.

Author Contributions: Conceptualization, S.P. and Y.P.; methodology, Y.P., V.S. and P.K.; validation, S.P., Y.P. and P.K.; formal analysis, P.K. and Y.Z.; investigation, P.K., M.K., A.K. and A.B.; resources, S.P. and Y.Z.; data curation, Y.P. and V.S.; writing—original draft preparation, P.K. and Y.P.; writing—review and editing, Y.P. and S.P.; supervision, S.P. and Y.P.; project administration, P.K.; funding acquisition, Y.Z. All authors have read and agreed to the published version of the manuscript.

Funding: The present work has been carried out with the financial support of the Strategic Academic Leadership Program “Priority 2030” at NUST “MISIS” (project K7-2023-013).

Data Availability Statement: Data sharing not applicable.

Conflicts of Interest: The authors declare no conflict of interest. The funders had no role in the design of this study, in the collection, analyses, or interpretation of data, in the writing of this manuscript, or in the decision to publish the results.

References

1. Venezuela, J.; Dargusch, M.S. Addressing the slow corrosion rate of biodegradable Fe-Mn: Current approaches and future trends. *Curr. Opin. Solid State Mater. Sci.* **2020**, *24*, 100822. [[CrossRef](#)]
2. Hermawan, H. *Biodegradable Metals—From Concept to Applications*; Springer: Berlin/Heidelberg, Germany, 2012. [[CrossRef](#)]
3. Park, J.; Lakes, R.S. *Biomaterials—An Introduction*; Springer: New York, NY, USA, 2007. [[CrossRef](#)]

4. Narushima, T. *Metals for Biomedical Devices*, 2nd ed.; Niinomi, M., Ed.; Elsevier: Amsterdam, The Netherlands, 2019; pp. 495–521. [[CrossRef](#)]
5. Witte, F. The history of biodegradable magnesium implants: A review. *Acta Biomater.* **2010**, *6*, 1680–1692. [[CrossRef](#)]
6. Seitz, J.-M.; Durisin, M.; Goldman, J.; Drelich, J.W. Recent advances in biodegradable metals for medical sutures: A critical review. *Adv. Healthc. Mater.* **2015**, *4*, 1915–1936. [[CrossRef](#)]
7. Li, C.; Guo, C.; Fitzpatrick, V.; Ibrahim, A.; Zwierstra, M.J.; Hanna, P.; Lechtig, A.; Nazarian, A.; Lin, S.J.; Kaplan, D.L. Design of biodegradable, implantable devices towards clinical translation. *Nat. Rev. Mater.* **2020**, *5*, 61–81. [[CrossRef](#)]
8. Heiden, M.; Walker, E.; Stanciu, L. Magnesium, Iron and Zinc Alloys, the Trifecta of Bioresorbable Orthopaedic and Vascular Implantation—A Review. *J. Biotechnol. Biomater.* **2015**, *5*, 178. [[CrossRef](#)]
9. Li, H.; Zheng, Y.; Qin, L. Progress of biodegradable metals. *Prog. Nat. Sci. Mater. Int.* **2014**, *24*, 414–422. [[CrossRef](#)]
10. Hyuk, S.; Jung, Y.; Kim, S.H. Current status and future direction of biodegradable metallic and polymeric vascular scaffolds for next-generation stent. *Acta Biomater.* **2017**, *60*, 3–22. [[CrossRef](#)]
11. Witte, F.; Hort, N.; Vogt, C.; Cohen, S.; Kainer, K.U.; Willumeit, R.; Feyerabend, F. Degradable biomaterials based on magnesium corrosion. *Curr. Opin. Solid State Mater. Sci.* **2008**, *12*, 63–72. [[CrossRef](#)]
12. Sezer, N.; Evis, Z.; Kayhan, S.M.; Tahmasebifar, A.; Koç, M. Review of magnesiumbased biomaterials and their applications. *J. Magnes. Alloys* **2018**, *6*, 23–43. [[CrossRef](#)]
13. Yang, H.; Jia, B.; Zhang, Z.; Qu, X.; Li, G.; Lin, W.; Zhu, D.; Dai, K.; Zheng, Y. Alloying design of biodegradable zinc as promising bone implants for load-bearing applications. *Nat. Commun.* **2020**, *11*, 401. [[CrossRef](#)]
14. Mostaed, E.; Sikora-Jasinska, M.; Mostaed, A.; Loffredo, S.; Demir, A.G.; Previtali, B.; Mantovani, D.; Beanland, R.; Vedani, M. Novel Zn-based alloys for biodegradable stent applications: Design, development and in vitro degradation. *J. Mech. Behav. Biomed. Mater.* **2016**, *60*, 581–602. [[CrossRef](#)] [[PubMed](#)]
15. Kraus, T.; Moszner, F.; Fischerauer, S.; Fiedler, M.; Martinelli, E.; Eichler, J.; Witte, F.; Willbold, E.; Schinhammer, M.; Meischel, M.; et al. Biodegradable Fe-based alloys for use in osteosynthesis: Outcome of an in vivo study after 52 weeks. *Acta Biomater.* **2014**, *10*, 3346–3353. [[CrossRef](#)] [[PubMed](#)]
16. Francis, A.; Yang, Y.; Virtanen, S.; Boccaccini, A.R. Iron and iron-based alloys for temporary cardiovascular applications. *J. Mater. Sci. Mater. Med.* **2015**, *26*, 138. [[CrossRef](#)] [[PubMed](#)]
17. He, J.; He, F.; Li, D.; Liu, Y.-L.; Liu, Y.Y.; Yea, Y.-J.; Yin, D.C. Advances in Fe-based biodegradable metallic materials. *RSC Adv.* **2016**, *6*, 112819–112838. [[CrossRef](#)]
18. Fantanariu, M.; Trinca, L.C.; Solcan, C.; Trofin, A.; Strungaru, S.; Şindilar, E.V.; Plavan, G.; Stanciu, S. A new Fe–Mn–Si alloplastic biomaterial as bone grafting material: In vivo study. *Appl. Surf. Sci.* **2015**, *352*, 129–139. [[CrossRef](#)]
19. Trinca, L.C.; Burtan, L.; Mareci, D.; Fernández-Perez, B.M.; Stoleriu, I.; Stanciu, T.; Stanciu, S.; Solcan, C.; Izquierdo, J.; Souto, R.M. Evaluation of in vitro corrosion resistance and in vivo osseointegration properties of a Fe–Mn–Si–Ca alloy as potential degradable implant biomaterial. *Mater. Sci. Eng. C* **2021**, *118*, 111436. [[CrossRef](#)]
20. Revie, W.R.; Uhlig, H.H. *Corrosion and Corrosion Control: An Introduction to Corrosion Science and Engineering*, 4th ed.; John Wiley and Sons Inc.: Hoboken, NJ, USA, 2008.
21. Lu, S.; Wang, Q.; Zhang, Y.; Li, H.; Feng, H.; Tan, L.; Yang, K. A novel biodegradable high nitrogen iron alloy with simultaneous enhancement of corrosion rate and local corrosion resistance. *J. Mater. Sci. Technol.* **2023**, *152*, 94–99. [[CrossRef](#)]
22. Otsuka, K.; Wayman, C.M. *Shape Memory Materials*; Cambridge University Press: Cambridge, UK, 1998; p. 284.
23. Drevet, R.; Zhukova, Y.; Malikova, P.; Dubinskiy, S.; Korotitskiy, A.; Pustov, Y.; Prokoshkin, S. Martensitic Transformations and Mechanical and Corrosion Properties of Fe–Mn–Si Alloys for Biodegradable Medical Implants. *Metall. Mater. Trans. A* **2018**, *49*, 1006–1013. [[CrossRef](#)]
24. Prokoshkin, S.; Pustov, Y.; Zhukova, Y.; Kadirov, P.; Dubinskiy, S.; Sheremetyev, V.; Karavaeva, M. Effect of thermomechanical treatment on functional properties of biodegradable Fe–30Mn–5Si shape memory alloy. *Metall. Mater. Trans. A* **2021**, *52*, 2024–2032. [[CrossRef](#)]
25. Prokoshkin, S.; Pustov, Y.; Zhukova, Y.; Kadirov, P.; Karavaeva, M.; Prosviryakov, A.; Dubinskiy, S. Effect of thermomechanical treatment on structure and functional fatigue characteristics of biodegradable Fe–30Mn–5Si 3 (wt.%) shape memory alloy. *Materials* **2021**, *14*, 3327. [[CrossRef](#)]
26. Sheremetyev, V.; Kudryashova, A.; Cheverikin, V.; Korotitskiy, A.; Galkin, S.; Prokoshkin, S.; Brailovski, V. Hot radial shear rolling and rotary forging of metastable beta Ti–18Zr–14Nb (at. %) alloy for bone implants: Microstructure, texture and functional properties. *J. Alloys Compd.* **2019**, *800*, 320–326. [[CrossRef](#)]
27. Kudryashova, A.; Sheremetyev, V.; Lukashevich, K.; Cheverikin, V.; Inaekyan, K.; Galkin, S.; Prokoshkin, S.; Brailovski, V. Effect of a combined thermomechanical treatment on the microstructure, texture and superelastic properties of Ti–18Zr–14Nb alloy for orthopedic implants. *J. Alloys Compd.* **2020**, *843*, 156066. [[CrossRef](#)]
28. Naizabekov, A.B.; Lezhnev, S.N.; Arbuz, A.S.; Panin, E.A. Obtaining of long-length rods with ultrafine-grained structure by the radial-shear rolling. *IOP Conf. Ser. Mater. Sci. Eng.* **2019**, *461*, 012065. [[CrossRef](#)]
29. Dobatkin, S.; Galkin, S.; Estrin, Y.; Serebryany, V.; Diez, M.; Martynenko, N.; Lukyanova, E.; Perezhogin, V. Grain refinement, texture, and mechanical properties of a magnesium alloy after radial-shear rolling. *J. Alloys Compd.* **2019**, *774*, 969–979. [[CrossRef](#)]
30. Stefanik, A.; Szota, P.; Mroz, S.; Bajor, T.; Dyja, H. Properties of the AZ31 magnesium alloy round bars obtained in different rolling processes. *Arch. Metall. Mater.* **2015**, *60*, 3001–3005. [[CrossRef](#)]

31. Gryc, A.; Bajor, T.; Dyja, H. The analysis of influence the parameters of rolling process in three high skew rolling mill of AZ31 magnesium alloy bars on temperature distribution. *Metallurgija* **2016**, *55*, 772–774.
32. Akopyan, T.; Aleshchenko, A.S.; Belov, N.A.; Galkin, S.P. Effect of Radial-Shear Rolling on the Formation of Structure and Mechanical Properties of Al-Ni and Al-Ca Aluminum-Matrix Composite Alloys of Eutectic Type. *Phys. Met. Metallogr.* **2018**, *119*, 241–250. [[CrossRef](#)]
33. Karpov, B.V.; Patrino, P.V.; Galkin, S.P.; Kharitonov, E.A.; Karpov, I.B. Radial-Shear Rolling of Titanium Alloy VT-8 Bars with Controlled Structure for Small Diameter Ingots (≤ 200 mm). *Metallurgist* **2018**, *61*, 884–890. [[CrossRef](#)]
34. Negodin, D.A.; Galkin, S.P.; Kharitonov, E.A.; Karpov, B.V.; Kharkovsky, D.N.; Dubovitskaya, I.A.; Patrino, P.V. Testing of the Technology of Radial-Shear Rolling and Predesigning Selection of Rolling Minimills for the Adaptable Production of Titanium Rods with Small Cross Sections Under the Conditions of the “CHMP” JSC. *Metallurgist* **2019**, *62*, 1143. [[CrossRef](#)]
35. Lopatin, N.V. Effect of hot rolling by screw mill on microstructure of a Ti-6Al-4V titanium alloy. *Int. J. Mater. Form.* **2013**, *6*, 459–465. [[CrossRef](#)]
36. Galkin, S.P. Theory and Technology of Stationary Helical Rolling of Billets and Bars of Low-Plasticity Steels and Alloys; Dissertation Abstract for the Degree of Doctor of Technical Sciences. Ph.D. Thesis, Moscow Institute, Moscow, Russia, 1998.
37. Manjunath, G.A.; Shivakumar, S.; Fernandez, R.; Nikhil, R.; Sharath, P.C. A review on effect of multi-directional forging/multi-axial forging on mechanical and microstructural properties of aluminum alloy. *Mater. Today Proc.* **2021**, *47*, 2565–2569. [[CrossRef](#)]
38. Zambrano, O.A.; Logé, R.E. Dynamic recrystallization study of a Fe-Mn-Si based shape memory alloy in constant and variable thermomechanical conditions. *Mater. Charact.* **2019**, *152*, 151–161. [[CrossRef](#)]
39. Kadirov, P.; Zhukova, Y.; Pustov, Y.; Karavaeva, M.; Sheremetyev, V.; Korotitskiy, A.; Shcherbakova, E.; Baranova, A.; Komarov, V.; Prokoshkin, S. Effect of plastic deformation in various temperature-rate conditions on structure and mechanical properties of biodegradable Fe-30Mn-5Si alloy. *Metall. Mater. Trans. A*, 2023; submitted.
40. Pustov, Y.; Zhukova, Y.; Malikova, P.; Prokoshkin, S.; Dubinskii, S. Structure and Corrosion-Electrochemical Behavior of Bioresorbable Alloys Based on the Fe–Mn System. *Prot. Met. Phys. Chem. Surf.* **2018**, *58*, 469–476. [[CrossRef](#)]
41. Sheremetev, V.A.; Akhmadkulov, O.B.; Komarov, V.S.; Korotitskii, A.V.; Lukashevich, K.E.; Galkin, S.P.; Andreev, V.A.; Prokoshkin, S.D. Thermomechanical Behavior and Structure Formation of Shape Memory Ti–Zr–Nb Alloy for Medical Applications. *Met. Sci. Heat Treat.* **2021**, *63*, 403–413. [[CrossRef](#)]
42. Winston, R.R. (Ed.) *Uhlig’s Corrosion Handbook*, 3rd ed.; John Wiley & Sons, Inc.: Hoboken, NJ, USA, 2011. [[CrossRef](#)]
43. *ASTM G31-21*; Standard Guide for Laboratory Immersion Corrosion Testing of Metals. ASTM International: West Conshohocken, PA, USA, 2021.
44. Isaev, N.I. *Theory of Corrosion Processes*; Metallurgiya: Moscow, Russia, 1997; p. 360. (In Russian)
45. Zhuk, N.P. *A Course in Corrosion Theory and Protection of Metals*; Metallurgiya: Moscow, Russia, 1976; p. 472. (In Russian)
46. Jiang, X.; Zhang, L.; Yin, L.; Yang, G.; Xie, J.; Zhang, L.; Lu, H.; Liang, D.; Deng, L. Corrosion behavior of fluorinated carbonyl iron-hydrophobic composites in neutral salt spray environment. *Corros. Sci.* **2023**, *210*, 110823. [[CrossRef](#)]
47. Sokol, I.Y.; Ulyanin, E.A.; Feldgandler, E.G. *Structure and Corrosion of Metals and Alloys, Atlas: A Handbook*; Metallurgy: Moscow, Russia, 1989; p. 400. (In Russian)
48. Hermawan, H.; Dube, D.; Mantovani, D. Degradable metallic biomaterials: Design and development of Fe–Mn alloys for stents. *J. Biomed. Mater. Res. Part A* **2010**, *93A*, 1–11. [[CrossRef](#)]
49. Xuemei, Z.; Yansheng, Z. Effect of ϵ -martensite on the electrochemical corrosion behavior of an Fe-Mn-Si shape memory alloy in aqueous solutions. *J. Mater. Sci. Lett.* **1997**, *16*, 1516–1517. [[CrossRef](#)]
50. Li, Y.; Jahr, H.; Pavanram, P.; Bobbert, F.S.L.; Puggi, U.; Zhang, X.-Y.; Pouran, B.; Leeftang, M.A.; Weinans, H.; Zhou, J.; et al. Additively manufactured functionally graded biodegradable porous iron. *Acta Biomater.* **2019**, *96*, 646–661. [[CrossRef](#)]
51. Obayi, C.S.; Tolouei, R.; Mostavan, A.; Paternoster, C.; Turgeon, S.; Okorie, B.A.; Obikwelu, D.O.; Mantovani, D. Effect of grain sizes on mechanical properties and biodegradation behavior of pure iron for cardiovascular stent application. *Biomater* **2016**, *6*, e959874. [[CrossRef](#)]
52. Rybalchenko, O.; Anisimova, N.; Martynenko, N.; Rybalchenko, G.; Belyakov, A.; Shchetinin, I.; Lukyanova, E.; Chernogorova, O.; Raab, A.; Pashintseva, N.; et al. Biocompatibility and Degradation of Fe-Mn-5Si Alloy after Equal-Channel Angular Pressing: In Vitro and In Vivo Study. *Appl. Sci.* **2023**, *13*, 9628. [[CrossRef](#)]

Disclaimer/Publisher’s Note: The statements, opinions and data contained in all publications are solely those of the individual author(s) and contributor(s) and not of MDPI and/or the editor(s). MDPI and/or the editor(s) disclaim responsibility for any injury to people or property resulting from any ideas, methods, instructions or products referred to in the content.